Frontiers in Computing and Intelligent Systems
ISSN: 2832-6024 | Vol. 6, No. 3, 2023

Blowout Fluid Velocity Measurement Method based on High-speed Sequence Images

Zijian Teng, He Zhang

School of Mechatronic Engineering, Southwest Petroleum University, Chengdu Sichuan, 610500, China

Abstract: Given the high-temperature and high-pressure environment after the blowout, the staff usually cannot calculate and analyze various blowout parameters at close range and thus take effective measures to control accidents quickly. In this paper, a blowout fluid velocity measurement method is proposed based on high-speed sequence images, and simulation experiments are conducted. The scene conditions of blowout accidents are simulated and analyzed. On this basis, cameras are adopted to shoot a large number of simulated blowout fluid videos from different angles under outdoor conditions. Afterward, the video is converted into a multi-frame image, and the blowout fluid image feature point detection and extraction model are established based on the orb (oriented fast and rotated brief) algorithm. On the feature points extracted by the model, the gms algorithm is used to match the features of the blowout fluid images in the front and back frames. Additionally, the wrong matching points are eliminated using the ransac (random sample consensus) algorithm, and the obtained feature point pairs are employed into the flow velocity calculation model for flow velocity calculation. The results demonstrate that the measured fluid velocity is more accurate. The method proposed in this study can provide reliable data support for early blowout emergency rescue.

Keywords: Blowout Velocity; Image Recognition; Feature Matching; Pinhole Imaging; Velocity Calculation.

1. Introduction

Generally, the operating environment of deep oil wells is extremely complex, with many unknown risks and changes. These factors reinforce the difficulty of mining in deep well environments. Safety risks are increasing with the increasing social demand for oil and natural gas and the continuous expansion of exploration and development fields. The occurrence of blowout accidents severely damages oil and gas resources, causes environmental pollution, and easily leads to fires, casualties, equipment damage, and even the scrapping of oil and gas wells. These also disrupt the normal production order [1,2]. When the blowout occurred, it is in a high-temperature and high-pressure environment with violent and harmful reactions. Hence, the staff are unable to calculate and analyze various blowout parameters at close range and take effective measures to control the accident quickly. In other words, in-depth research on measurement techniques and equipment such as blowout fluid parameters should be conducted in-depth research on measurement techniques and equipment such as blowout fluid parameters, which is of great significance for early blowout emergency rescue [3-6].

Dong et al. carried out the research investigated on the equilibrium state of the underwater emergency sealing device, and simulated the analysis model, and obtained revealed the relationship between its flow velocity and the lifting force [7]. Jia et al. utilized the ultrasonic time-of-flight method to measure the fluid flow, demonstrating that the ultrasonic propagation time and the horizontal component of the propagation displacement were inversely and directly proportional to the flow velocity, respectively. They also calibrated the flow measurements using the tangent of refraction versus ultrasonic transit time [8]. Wang et al. designed a fluid flow rate measurement system based on the *lms* least mean square algorithm and a single-chip microcomputer as the main controller, and verified the feasibility of the system with actual test results [9]. Li et al. theoretically and numerically studied the lift-off distance and blowout limit of the boundary layer diffusion flame, and deduced the explicit solution of the flame lift-off distance and critical blowout limit [10]. Based on the robot volume *ptv* measurement method, C Jux et al. proposed an experimental method to measure the time-averaged fluid flow pressure on the surface of a general three-dimensional object for evaluating the pressure distribution on the surface of the object [11]. Sara Rashed et al. established a new approach to measure each component in oil-gas-water mixtures by deploying devices such as biplane electrical resistance tomography sensors, gradient pressure gauges, and flow density meters, so as to estimate fluid volumetric flow rates. They further deduce the water content and gas volume fraction based on the method [12]. With cameras, Wu Zhou et al. obtained the size and position of each imaged droplet using the depth-from-focus method and introduced a simple algorithm to estimate the size and position from the two-camera images. The effect of the algorithm on the sensitivity of various system parameters was investigated through simulations using synthetic images, measurements with calibrated equipment, and measurements performed in a sparse spray [13]. Moreover, B. Rengel et al. presented an advanced equation to predict the self-extinguishing conditions of jet flames after blowout accidents and verified that it can determine the extinguishing speed of jet flames involving various gas fuels, wind conditions, flow regimes, and directions [14]. Bang et al. researched the effect of pressure on the characteristics of the rising flame in the co-flow of propane fuel, discovering that the flame rising height, ground clearance height, and ejection velocity all decreased to varying degrees as the test pressure decreased [15].

After the fluid is ejected, the ground staff cannot approach and detect fluid parameters owing to the strong pressure and high temperature of the formation. Moreover, there is currently no instrument that can measure the blowout velocity at close range. In this paper, a blowout fluid velocity measurement method based on high-speed sequence images was proposed to quickly measure the flow velocity of blowout

fluid in the early stage of blowout accidents. This provides suggestions for well site staff to rapidly judge dangerous situations.

2. Fluid Jet Flow Analysis and Research Ideas

2.1. Analysis of Fluid Jet Flow Movement

Generally, free jets have the property of jetting into bundles, and a bundled jet is formed above the spout. There is a large velocity gradient between the ejected fluid and the surrounding medium, and momentum exchange occurs between fluid particles and between adjacent fluid particles. The momentum of the free jet along the length direction remains unchanged, indicating that after the mass point of the ejected medium collides with the surrounding medium, the collided mass point obtains momentum and moves, though the momentum decreases. As a result, the sum of the momentum of the two remains constant. The reduction of kinetic energy is caused by the collision between the fast-moving gas and the slow-moving medium that is driven up, where the lost kinetic energy is converted into heat. As the height and diameter of the jet increase, the jet transfers part of its momentum to the incoming fluid, and thus the velocity of the jet gradually decreases. Eventually, all the momentum of the jet disappears in the space fluid [16]. In order to simplify the complex medium motion of well jet flow, subsequent experiments used water flow to replace the well jet fluid. After the blowout jet forms a stable flow state, its jet shape and flow velocity distribution are illustrated in Figure 1.

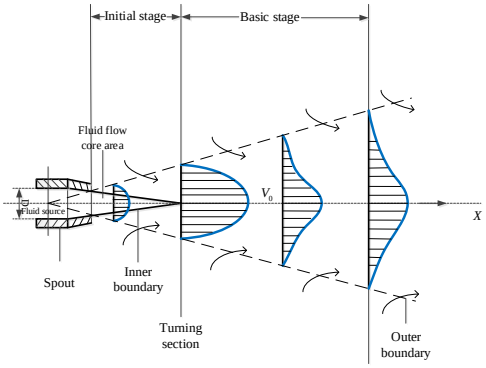

Fig 1. Velocity distribution of well jet flow

In Figure 1, the jet boundary is regarded as a linear diffusion interface according to the statistical average significance. The velocity evolution process of the water jet is that the water flow is ejected from the spout with a diameter D at the initial velocity V_0. When it moves along the *X-axis* for a certain distance, momentum exchange occurs between fluid particles, the jet boundary gradually widens, the velocity of the main body of the jet attenuates, and thus the area that still maintains the initial velocity gradually becomes smaller. These results are induced by the large velocity gradient between the ejected fluid and the surrounding medium. Generally, the initial velocity boundary of the jet is considered the inner boundary of the jet. At a certain height, the jet boundary layer expands to the central axis of the jet. At this time, only the velocity on the centerline of the jet maintains the initial velocity V_0, and the cross-section at the centerline is viewed as a turning section. In other words, starting from this turning section, the surrounding fluid is entrained and drawn to the ejection direction to accelerate, while the jet boundary becomes wider and wider. Furthermore, the jet flow section from the wellhead to the turning section is defined as the jet flow initial section, the jet flow center velocity in this section is equal to V_0, and the jet flow core area has an initial velocity V_0. The part above the turning section is defined as the basic section of the jet flow. This section moves farther away from the turning section along the *X-axis*, and the center velocity is continuously attenuated along the central axis. The jet source opening angle is 18^°~26^° [17-19].

2.2. Research Ideas

The overall research approach of this article is to simulate and analyze the on-site conditions of a blowout accident, using water flow to simulate the blowout fluid. Utilize high-speed cameras to capture a large number of simulated blowout fluid videos outdoors, then convert the videos into multiple frames of images, and establish an image feature point detection and extraction model based on *orb* (oriented fast and rotated brief) algorithm. On the feature points extracted from the model, *gms* algorithm is used to achieve feature matching of fluid images before and after frames, and *ransac* (random sample consumus) algorithm is used to eliminate erroneous matching points. The final feature point pairs are substituted into the flow rate calculation model for flow rate calculation and compared with the standard flow rate for error analysis. The research idea of this paper is shown in Figure 2.

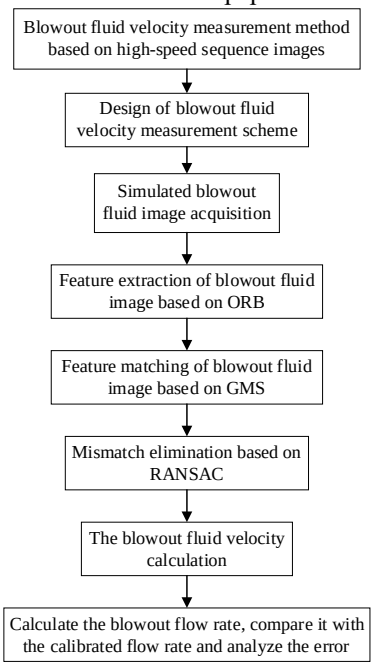

Fig 2. Research plan

3. Image Processing Model Establishment

3.1. ORB Feature Detection Algorithm

Orb is an image feature detection algorithm optimized based on the *fast* key point detector and the *brief* descriptor. *Fast* is widely applied for its high efficiency in feature point detection, while it is deficient in directionality. Therefore, a simple and effective method of intensity center-of-mass angle orientation measurement is introduced in the *orb* algorithm to equip the key points of the *orb* with direction components and rotation invariance. Moreover, a scale pyramid is adopted to generate *fast* features at each layer of the pyramid, contributing to the scale invariance of the *orb* algorithm [20].

The *orb* algorithm adopts the gray-scale centroid method

to determine the main direction of the feature point. Firstly, the gray-scale centroid *C* in the neighborhood of the feature point is determined. Then, the geometric center *O* of the local area of the feature point is constructed to point to the direction vector of the gray-scale centroid *C*, expressed as:17,8.5

$$m_{pq} = \sum_{x,y} x^p y^p I(x,y) \quad (1)$$

where $I(x,y)$ represents the gray value at the pixel point (x,y).

At this time, the centroid of the image block is obtained by equation (2):

$$C = \left(\frac{m_{10}}{m_{00}}, \frac{m_{01}}{m_{00}}\right) \quad (2)$$

where m_{00} denotes the zero moment; m_{01} and m_{10} indicate the first-order moment.

The feature point direction θ is defined as:

$$\theta = arctan\left(\frac{m_{01}}{m_{10}}\right) \quad (3)$$

After extracting oriented *fast* key points, its descriptor is calculated for each point. *Orb* uses a modified *brief* feature description, where *brief* is a binary descriptor whose description vector consists of many zeros and ones. The zeros and ones encode the size relationship between two random pixels (such as p and q) near key points. If p is larger than q, one is taken; otherwise, zero is taken. If 128 such p and q are taken, it ends up with a 128-dimensional vector consisting of 0 and 1. *brief* takes the comparison of randomly selected points, which is fast and easy to store attributed to the use of a binary representation, and is suitable for real-time image matching. In this study, 256 was selected as the feature descriptor string length [21].

3.2. GMS Feature Matching Algorithm

The *gms* (grid-based motion statistics) algorithm can improve the efficiency of the operation while ensuring the matching effect. The lack of apparent correct matches is induced by the difficulty in distinguishing between correct and incorrect matches, rather than the low number of matching pairs. Since the feature points in the correctly matched neighborhood frequently maintain geometric consistency, the correct and wrong matches can be distinguished by evaluating the number of matching points contained in the adjacent area of the matching pair to be judged [22], as detailed in Table 1.

Table 1. GMS algorithm solves the following problems

Problem	Solution
Grid scoring	Divide the image into 20*20, numbered 1-400
Robust Neighbor Grouping	The eight squares surrounding a square serve as neighbors, with rotation and scale provided.
Appropriate number of grids	20*20 is suitable for 10000 feature points. More feature points can divide more grids
Separation of correct and false matches by thresholding	The threshold is determined by the preset threshold and the average number of features of the 9 adjacent squares.

The sum of the total number of matches in the grid corresponding to the nearest neighbors (9 grids) in the other image corresponding to the grid corresponding to the nearest neighbors is calculated, written as:

$$S_{ij} = \sum_{k=1}^{K=9} \left| X_i k_j k \right| \quad (4)$$

The exact and false matches are divided as:

$$\text{cell} - \text{pair}\{i,j\} \begin{cases} \text{True}, & \text{if } S_{ij} > \tau_i = \alpha\sqrt{n_i} \\ \text{Flase}, & \text{otherwise} \end{cases} \quad (5)$$

where n_i denotes the average number of features mentioned in the table, and α represents a hyperparameter, which is generally set to 4~6.

3.3. Random Sampling Consensus (RANSAC) Algorithm

The random sample consensus (*ransac*) algorithm is a model-based robust iterative estimation algorithm, which can calculate and give a reasonable model parameter set in the case of high outliers in the data set. The calculation process is illuminated in Figure 3. The *ransac* algorithm is used when most of the observations match a model, while a small proportion of data (outliers) are distributed in the data space in the model, and the outliers deviate from the normal data by a small margin. The application is the elimination and correction of mismatched points after image feature matching [23].

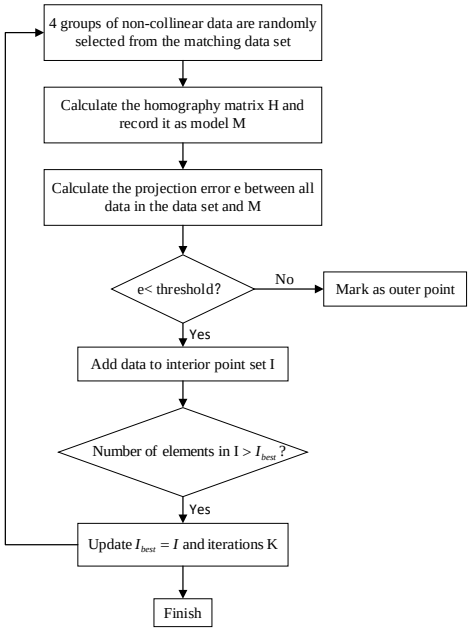

Fig 3. ransac algorithm flow chart

In, *opencv* the *ransac* algorithm eliminates the mismatched pairs in the existing image feature matching pairs by finding the best homography matrix $H(3 \times 3)$. The pixel point transformation relationship of the two images described by H is described as:

$$s\begin{bmatrix} x' \\ y' \\ 1 \end{bmatrix} = \begin{bmatrix} h_{11} & h_{12} & h_{13} \\ h_{21} & h_{22} & h_{23} \\ h_{31} & h_{32} & h_{33} \end{bmatrix} \begin{bmatrix} x \\ y \\ 1 \end{bmatrix} \quad (6)$$

where (x,y) represents the corner position of the previous image, (x',y') indicates the corner position of the next image, and s refers to the scale factor. $h_{33} = 1$ is the normalized matrix.

Therefore, there are 8 unknown parameters in H, and at least 8 linear equations need to be established for a solution, namely, at least 4 matching pairs. In this paper, 4 groups of non-collinear data are randomly selected from the matching data set and then employed to calculate the homography matrix H. Finally, the matching point logarithm and projection error that satisfy this model are calculated, that is, the cost function e. The corresponding cost function is the smallest when the model reaches the optimum.

$$e = \sum_{i=1}^{n}\left[\left(x_i' - \frac{h_{11}x_i+h_{12}y_i+h_{13}}{h_{31}x_i+h_{32}y_i+h_{33}}\right)^2 + \left(y_i' - \frac{h_{21}x_i+h_{22}y_i+h_{23}}{h_{31}x_i+h_{32}y_i+h_{33}}\right)^2\right] \quad (7)$$

3.4. Establishment of Flow Velocity Calculation Model

In the current development of camera technology, pinhole imaging is still the core idea of camera imaging, where the pinhole imaging model is generally adopted [24]. The principle of pinhole imaging is exhibited in Figure 4. Before the blowout velocity is calculated by applying the pinhole imaging method, the internal and external parameters of the camera needed to be first determined, as well as converting the external parameters from the pixel coordinate system to the world coordinate system [25].

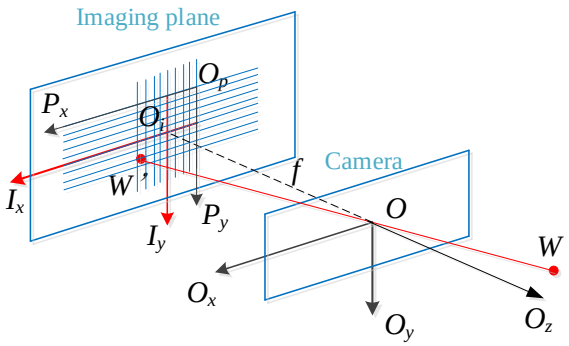

Fig 4. Pinhole imaging model

In Figure 4, the camera coordinate system takes O as the camera optical center, the O_z, O_x and O_y axis as the optical axis, the horizontal axis, and the vertical axis, respectively. The coordinate system composed of the coordinate origin O_i, the abscissa I_x, and the ordinateI_y is the image coordinate system, where I_x and I_y are parallel to O_x and O_y in the camera coordinate system, respectively and the distance OO_i between the optical center O of the camera coordinate system and the origin O_i of the image coordinate system is the focal length f. The coordinate system consisting of the coordinate origin O_p, the abscissa P_x, and the ordinate P_x is a pixel coordinate system, where any point (P_{xi}, P_{yi}) in the coordinate system represents the coordinates of a pixel point in the image. However, the pixel coordinates should be converted to image coordinates since the pixel coordinate system failed to reflect the specific position of the target in the image [26]. It is assumed in this paper that the pixel coordinates of O_i in the image coordinate system are (P_{xo}, P_{yo}), and the pixel specification of the photosensitive device in the camera is $d_x \times d_y$. Thus, the conversion relationship between the pixel coordinate system and the image coordinate system is obtained, expressed as:

$$\begin{cases} \boldsymbol{I_x = (P_x - P_{x0})dx} \\ \boldsymbol{I_y = (P_y - P_{y0})dy} \end{cases} \quad (8)$$

The homogeneous equation of its matrix is:

$$\begin{bmatrix} I_x \\ I_y \\ 1 \end{bmatrix} = \begin{bmatrix} dx & 0 & -P_{x0}dx \\ 0 & dy & -P_{y0}dy \\ 0 & 0 & 1 \end{bmatrix} \begin{bmatrix} P_x \\ P_y \\ 1 \end{bmatrix} \quad (9)$$

The image formed in the image is set as point $W'(I_x, I_y)$ when the W coordinate of a point of the object in the camera coordinate system is (O_x, O_y, O_z). Subsequently, the conversion relationship between the image coordinate system and the camera coordinate system is described as:

$$\begin{bmatrix} O_x \\ O_y \\ O_z \\ 1 \end{bmatrix} = \begin{bmatrix} O_z/f & 0 & 0 \\ 0 & O_z/f & 0 \\ 0 & 0 & O_z \\ 0 & 0 & 1 \end{bmatrix} \begin{bmatrix} I_x \\ I_y \\ 1 \end{bmatrix} \quad (10)$$

The relationship with the pixel coordinate system is written as:

$$\begin{bmatrix} O_x \\ O_y \\ O_z \\ 1 \end{bmatrix} = \begin{bmatrix} (O_z dx)/f & 0 & (-O_z P_{x0} dx)/f \\ 0 & (O_z dy)/f & (-O_z P_{y0} dy)/f \\ 0 & 0 & O_z \\ 0 & 0 & 1 \end{bmatrix} \begin{bmatrix} P_x \\ P_y \\ 1 \end{bmatrix} \quad (11)$$

When camera calibration is performed, the obtained camera intrinsic parameters are denoted as k_x, k_y and P_{x0}, P_{y0}, where $k_x = f * (1/dx)$, $k_y = f * (1/dy)$.

When the target scene is parallel to the camera plane, the target scene point $W_0 = (O_{x0}, O_{y0}, O_{z0})$ moves to $W_1 = (O_{x1}, O_{y1}, O_{z1})$, which is equivalent to moving from $W'_0 = (P_{xo}, P_{yo})$ to $W_1 = (P_{x1}, P_{y1})$ on the image. Based on the mapping relationship, equation (12) is derived as:

$$\begin{cases} P_{x1} - P_{x0} = \frac{k_x(O_{x1} - O_{xo})}{O_z} \\ P_{y1} - P_{y0} = \frac{k_y(O_{y1} - O_{yo})}{O_z} \end{cases} \quad (12)$$

The ratio of the pixel to the actual distance can be deduced after calibrating k_x and k_y by the camera and calculating the distance O_z between the camera and the jet surface. Assuming that the pixel moving by the object on the imaging plane is $(\Delta m, \Delta n)$, the actual moving distance ΔY should be:

$$\Delta Y = \sqrt{\left(\frac{\Delta m O_z}{k_x}\right)^2 + \left(\frac{\Delta n O_z}{k_y}\right)^2} \quad (13)$$

Finally, the time interval Δt of the front and rear frames is deduced according to the frame rate of the camera. Hence, the initial velocity of the well jet can be calculated by:

$$\begin{cases} \Delta Y = \omega_0 \Delta t - \frac{1}{2} g(\Delta t)^2 \\ \omega_0 = (\Delta Y + \frac{1}{2} g(\Delta t)^2)/\Delta t \end{cases} \quad (14)$$

In this paper, the calculation of flow velocity is based on the front and rear frame images, and its feature points are extracted and matched. With the method of physical size conversion coefficient and lens imaging, the flow velocity is calculated through the pixel difference of the feature point displacement of the front and rear frame images, as well as the time difference between the front and rear frames.

4. Experimental Analysis and Evaluation

4.1. Simulated Blowout Fluid Velocity Measurement Scheme

In this paper, two high speed industrial cameras are adopted as simulated blowout fluid image acquisition devices. The specific flow rate measurement process is detailed as follows. 1) In an outdoor environment, two cameras are set at an angle of 90° to the blowout target line; 2) the lens parallel are set to the jet fluid axis section; 3) the camera and blowout simulation parameters of the device are set; 4) acquisition of blowout video; 5) after the video of the blowout fluid is collected by the camera, the video is transmitted to the host

computer through the local area network, and the blowout video is processed into an image sequence on the host computer for subsequent image feature detection operations.

The blowout fluid feature points on the sequence images are extracted using the image extraction algorithm. Afterward, the key feature points are matched with the feature-matching algorithm. Next, the displacement difference between the front and rear feature matching points is calculated following the matched key feature points, and the blowout fluid velocity calculation is further realized under the time difference. Figure 5 exhibits a block diagram of blowout fluid velocity measurement.

During the blowout video collection process, two WP-GX180 cameras were placed in two orientations at an angle of 90° to the blowout target line. The blowout video acquisition was performed under the background optimization and the natural background while the focal length f of the two cameras, the image pixel size, the object distance d, and the camera height H remained constant. The acquisition scheme and parameter settings are listed in Table 2. Afterward, the collected blowout video was processed into continuous frame images for flow velocity calculation.

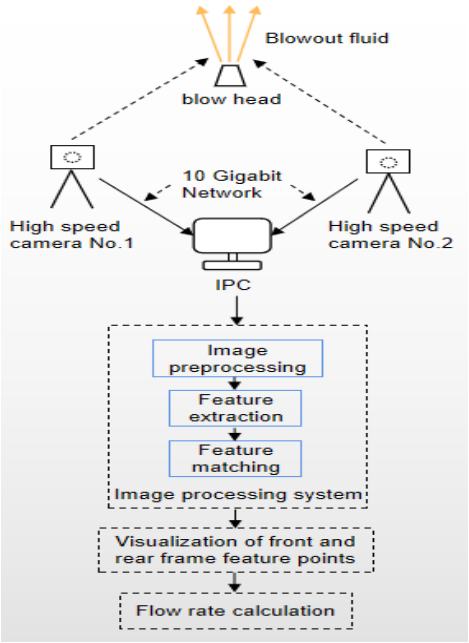

Fig 5. Blowout fluid velocity measurement block diagram

Table 2. Blowout video acquisition scheme

Camera 1: Video frame rate:610fps,1600*1100			Camera 2: Video frame rate:610fps,1600*1100		
Object distance: d=245cm; Camera height: H=100.5cm	Focal distance: f_1=35mm Total height: h=165cm	Speed 1(water pressure:4MPa)	Object distance: d=244cm; Camera height: H=97cm	Focal distance: f_1=35mm Total height: h=137cm	Speed 1(water pressure:4MPa)
		Speed 2(water pressure:3MPa)			Speed 2(water pressure:3MPa)
		Speed 3(water pressure:2MPa)			Speed 3(water pressure:2MPa)
		Speed 4(water pressure:1MPa)			Speed 4(water pressure:1MPa)
	Focal distance: f_2=75mm Total height: h=107.5cm	Speed 1(water pressure:4MPa)		Focal distance: f_2=75mm Total height: h=93cm	Speed 1(water pressure:4MPa)
		Speed 2(water pressure:3MPa)			Speed 2(water pressure:3MPa)
		Speed 3(water pressure:2MPa)			Speed 3(water pressure:2MPa)
		Speed 4(water pressure:1MPa)			Speed 4(water pressure:1MPa)

4.2. Blowout Simulation

Through the analysis of the actual blowout characteristics, the blowout simulation test was conducted using the self-developed blowout simulation device. Above all, the power supply, fluid tank, centrifugal pump, mass flow meter, nozzle, host computer, and other equipment were connected. Then, the two cameras were placed in two orientations, respectively at an angle of 90° to the intersection point of the nozzle connection point of the blowout simulation device to collect blowout fluid video. Figure 6 and Figure 7 display the blowout fluid video collection scheme and camera site layout, respectively.

Fig 6. Flow of video acquisition of simulated blowout fluid

During the experiment, the camera captures video images of the blowout fluid, as presented in Figure 8. The video image transmits the blowout fluid video data acquired to the host computer through wireless transmission, and the video

data is processed into a continuous frame image sequence. The processed image sequences are displayed in Fig. 9(a), (b) and Fig. 10(a), (b) for the image sequences under background optimization and the natural background of camera 1 and camera 2, respectively.

Fig 7. Camera site layout

Fig 8. Blowout fluid image

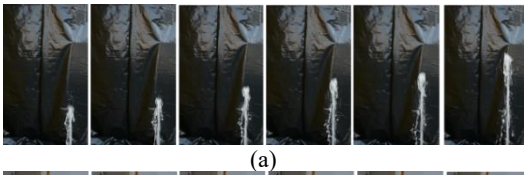

(a)

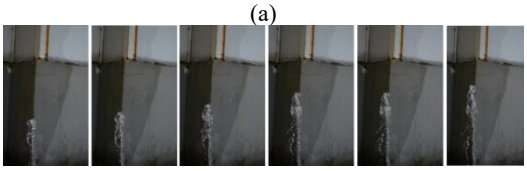

(b)

Fig 9. Camera 1 image sequence

(a)

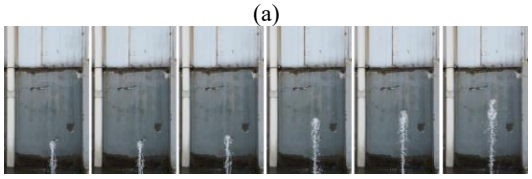

(b)

Fig 10. Camera 2 image sequence

4.3. Blowout Fluid Velocity Calculation

The blowout fluid image data obtained by camera 1 and camera 2 were selected to simulate the image processing model proposed in this paper, so as to verify the reliability of the image obtained by the blowout simulation experiment and the accuracy of the image processing model in this paper.

4.3.1. Fluid Image Feature Extraction

The *orb* algorithm proposed in this paper is utilized to perform feature detection on the blowout fluid pictures of camera 1 and camera 2. The results are exhibited in Figure 11. (a), (b).

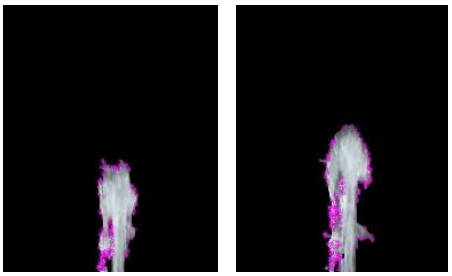

(a) Camera 1 blowout fluid feature detection

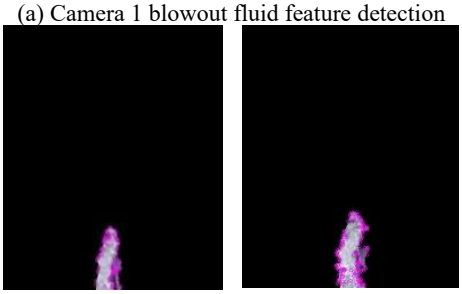

(b) Camera 2 blowout fluid feature detection

Fig 11. Blowout fluid characteristic detection results

4.3.2. Fluid Image Feature Matching

After the blowout fluid image feature point detection, the blowout fluid image feature matching based on gms and ransac is performed with the detected feature point descriptor. Figure 12 renders the feature-matching results of the two frames before and after the blowout fluid image of camera 1 and camera 2.

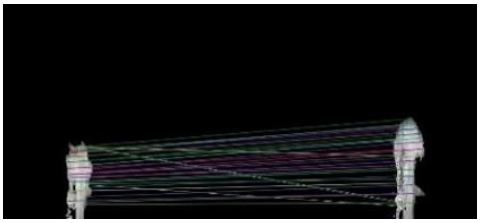

(a)

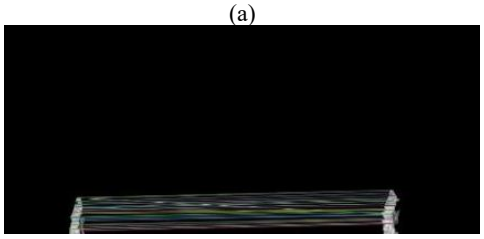

(b)

Fig 12. Blowout fluid feature matching results

4.3.3. Calculation of Fluid Velocity

In this paper, the initial velocity of the blowout fluid of 3 groups of different initial velocities taken when the focal length of the camera is 35mm and 75mm in the blowout simulation device is calculated. The performance of the flow velocity calculation method proposed in this paper is analyzed with respect to the calibrated flow velocity of the mass flow meter. The pixel position coordinates of feature points are illustrated in Figures 13 and 14.

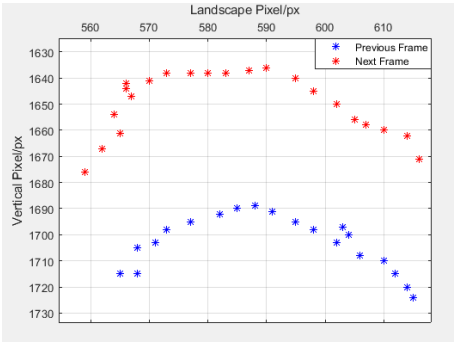

(a)

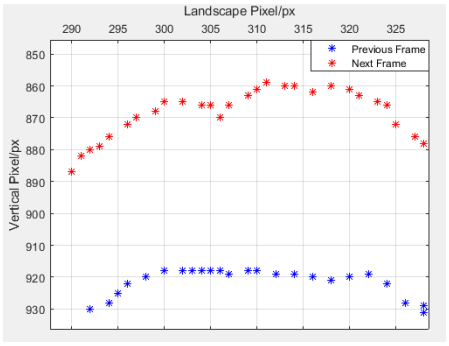

(b)

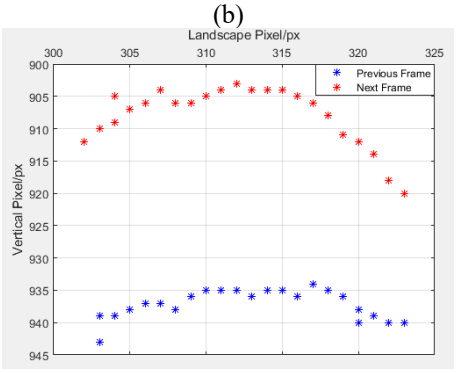

(c)

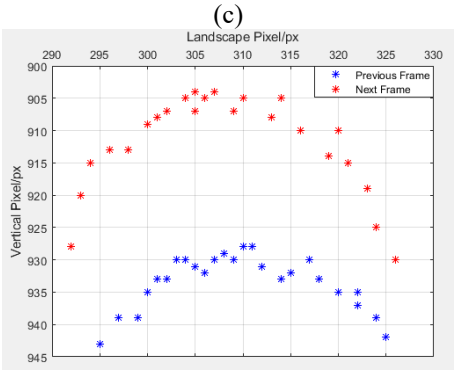

(d)

Fig 13. Pixel distribution of feature points on the upper boundary of well jet flow when the camera focal length is 35 mm

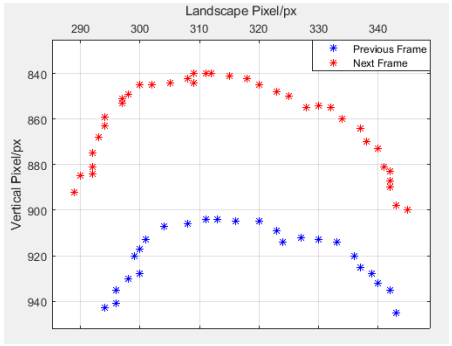

(a)

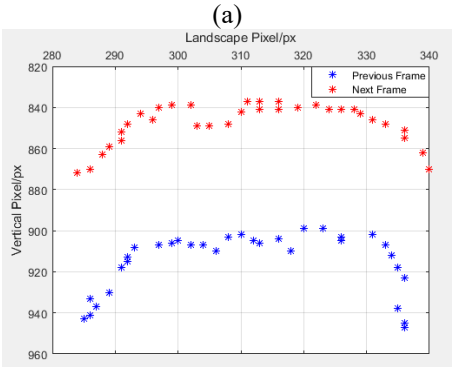

(b)

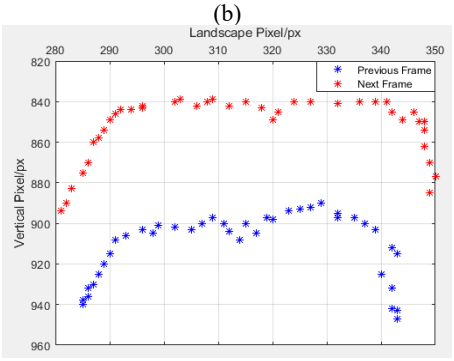

(c)

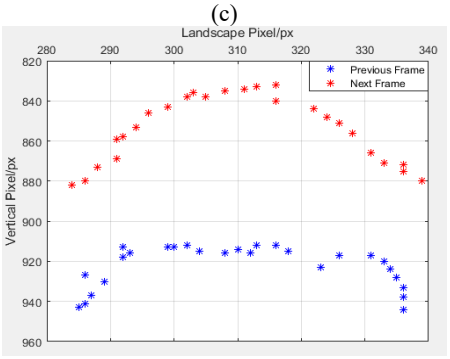

(d)

Fig 14. Pixel distribution of feature points on the upper boundary of well jet flow when the camera focal length is 75 mm

Table 3. Calculation results of blowout velocity

Experimental Samples	f=35mm			f=75mm		
	Displacement ($m*10^{-2}$)	Time ($s*10^{-3}$)	Velocity (m/s)	Displacement ($m*10^{-2}$)	Time ($s*10^{-3}$)	Velocity (m/s)
Sample 1	3.553	1.7	21.02	3.606	1.8	20.93
Sample 2	3.026	1.8	16.78	3.584	2.1	18.12
Sample 3	2.683	1.7	15.63	3.460	2.5	14.63
Sample 4	2.075	1.8	12.07	3.305	2.8	12.69

Figures 13 and 14 detail the pixel movement of the feature points at the moment before and after the blowout fluid jet.

The vertical displacement distance of the feature point pixel is calculated following the feature-matching pairs of the front and back frames. Then, the pinhole imaging method is adopted to obtain the actual blowout fluid displacement distance. Since the blowout image is obtained by video conversion, the time interval of the blowout images of the previous and subsequent frames can be obtained. Therefore, the blowout velocity can be calculated through equation (14), as listed in Table 3.

4.4. Comparative Analysis of Model Errors

After the calculation of the blowout fluid flow rate by image processing combined with the pinhole imaging method, the fluid flow rate recorded by the mass flow meter in the blowout simulation device was converted into the nozzle flow rate and taken as the calibration for the well blowout fluid flow rate to verify the accuracy of calculated blowout fluid flow rate. The comparison results of the calculated blowout fluid flow rate value and the calibrated flow rate value are provided in Table 4. Figure 15 presents a comparison chart of the accuracy of the two.

Table 4. Comparison results of flow rate accuracy of blowout fluid at different focal lengths

Experimental Samples	Calibrated flow rate (m/s)	f=35mm		f=75mm	
		Velocity (m/s)	Accuracy (%)	Velocity (m/s)	Accuracy (%)
Sample 1	20.28	21.02	96.48	20.93	96.89
Sample 2	17.84	16.78	94.06	18.12	98.45
Sample 3	14.92	15.63	95.46	14.63	98.06
Sample 4	12.45	12.07	96.95	12.69	98.11

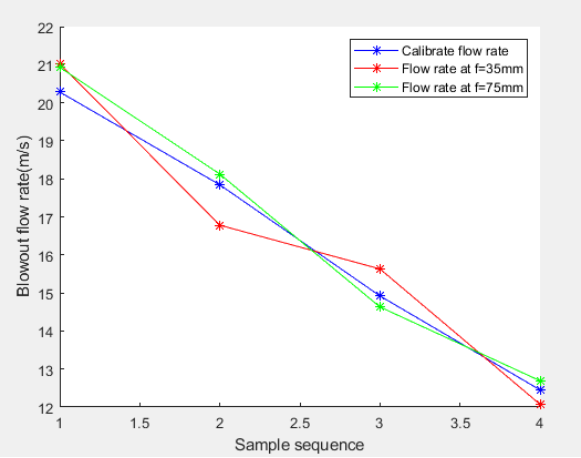

Fig 15. Comparison of blowout fluid flow velocity and calibration flow velocity at different focal lengths

From Table 4 and Figure 15, it can be concluded that when the camera focal length f=35mm, its flow rate value is relatively close to the calibrated flow rate value, and its calculation accuracy is the lowest at 94.06% and the highest at 96.95%; When the focal length of the camera is f=75mm, its flow rate value is closest to the calibrated flow rate value, and its calculation accuracy is the lowest at 96.89% and the highest at 98.45%. From this, it can be concluded that at a focal length of f=35mm, the clarity of the captured fluid image is low due to the small focal length, which has a certain degree of impact on the recognition and extraction of image feature points, and the accuracy of flow velocity measurement is low; When the focal length f=75mm, the accuracy of the calculated blowout fluid velocity value is relatively high.

5. Summary

Considering that it is difficult to collect on-site blowout pictures, a self-developed blowout simulation device was employed in this study to simulate blowout fluid and collect pictures. The characteristics of the blowout fluid were analyzed, and the initial velocity of the jet at the blowout nozzle was determined as the target for calculation. On this basis, the *orb-gms-ransac* blowout image feature point matching method was proposed. With the pinhole imaging method, the matching pair of upper edge features of the well blowout flow was utilized as the key point to calculate the blowout fluid flow rate. Finally, the cause of the error was analyzed by comparing it with the flow rate measured by the mass flow meter. The results unveiled that the flow rate of blowout fluid calculated by this image processing model has high accuracy and low error. This provides a reference for the well site staff to quickly judge the danger in the early stage of blowout accidents and thus is of great significance to the emergency rescue of an early blowout.

References

[1] Z. F. Liu, J. Q. Liu, Q. Z. Zhu and W. Wu. The weathering of oil after the Deepwater Horizon oil spill: insights from the chemical composition of the oil from the sea surface, salt marshes and sediments[J]. Environmental Research Letters 2012 Vol. 7 Issue 3.

[2] R. Islam, F. Khan and R. Venkatesan. Real time risk analysis of kick detection: Testing and validation[J]. Reliability Engineering & System Safety 2017 Vol. 161 Pages 25-37.

[3] LIU Z, MA Q, CAI B, LIU Y, ZHENG, C. Risk assessment on deepwater drilling well control based on dynamic Bayesian network[J]. Process safety and environmental protection, 2021,149: 643-654.

[4] MA Q, ZHANG L. CFD simulation study on gas dispersion for risk assessment: A case study of sour gas well blowout[J]. Safety science, 2011,49(8-9): 1289-1295.

[5] ZHU Y, CHEN G. Simulation and assessment of SO2 toxic environment after ignition of uncontrolled sour gas flow of well blowout in hills[J]. Journal of hazardous materials,2010,178(1-3): 144-151.

[6] J. Y. Xie, X. Y. Zhang, Y. W. Tang, Y. Wang, Q. Q. Shao and B. Yu. Transient simulation of the blowing-out process of the air pockets in vertical wellbore[J]. Applied Thermal Engineering 2014 Vol. 72 Issue 1 Pages 97-103.

[7] X. Dong, C. Zhang, C. Gu, J. Yang, M. Wang, Y. Wang. Balance analysis of the lowering process of 3000m subsea emergency well sealing device[J]. China Offshore Oil and Gas,2020,32(05):114-119.

[8] H. Jia, C. Wang, R. Dang. Influence of fluid velocity on ultrasonic flow measurement accuracy and its calibration[J]. Journal of Instrumentation,2020,41(07).

[9] R. Wang, M. Zhou, P. Yan, K. Zhang. Fluid Velocity Measurement System Based on LMS Algorithm[J]. Instrument Technique and Sensor, 2015(06):63-65.

[10] S. P. Li, Q. Yao, C. K. Law, W. K. Liang and J. K. Zhuo. Liftoff and blowout of the Emmons flame: Analysis of the triple flame[J]. Combustion and Flame 2020 Vol. 215 Pages 184-192.

[11] C. Jux, A. Sciacchitano and F. Scarano. Flow pressure evaluation on generic surfaces by robotic volumetric PTV[J]. Measurement Science and Technology 2020 Vol. 31 Issue 10.

[12] S. Rashed, Y. Faraj, M. Wang and S. Wilkinson. Electrical resistance tomography-based multi-modality sensor and drift flux model for measurement of oil-gas-water flow[J]. Measurement Science and Technology 2022 Vol. 33 Issue 9.

[13] W. Zhou, C. Tropea, B. T. Chen, Y. K. Zhang, X. Luo and X. S. Cai.Spray drop measurements using depth from defocus[J]. Measurement Science and Technology 2020 Vol. 31 Issue 7.

[14] RENGEL B, PALACIOS A. Analysis of experimental blowout velocities of jet flames[J]. Combustion and flame, 2020,213: 237-239.

[15] BANG S, LEE B, CHUNG S. Effect of pressure on the characteristics of lifted flames[J]. Proceedings of the combustion institute, 2019,37(2): 2013-2020.

[16] C. Hotz, M. Haas, S. Wachter, S. Fleck and T. Kolb. Two-phase free jet model of an atmospheric entrained flow gasifier[J]. Fuel 2021 Vol. 304.

[17] H. T. Peng, W. Nie, S. B. Zhang, W. M. Cheng, Q. Liu, C. Guo, et al. Research on negative pressure jet dust-removal water curtain technology for coal mine cleaner production[J]. Fuel 2022 Vol. 310.

[18] S. Pucci, G. Poletto, A. C. Sterling and M. Romoli. Physical parameters of standard and blowout jets[J]. Astrophysical Journal. 2013 Vol. 776 Issue 1.

[19] Z. Liu, Y. Zhang, Y. Zheng, F. Wang, X. Qian, D. Zhang, P. Huang, Q. Li, C. Feng. Characteristics of Blowout Flow Field in Natural Gas Wells Containing CO2[J]. Petroleum Exploration and Development, 2011,38(01):90-96.

[20] Chuan L, Wei Y, Panling H and Jun Z. Overview of Image Matching Based on ORB Algorithm[J]. Journal of Physics: Conference Series, Volume 1237, Issue 3.

[21] E. Rublee, V. Rabaud, K. Konolige, G. Bradski and Ieee. ORB: an efficient alternative to SIFT or SURF[C]. IEEE International Conference on Computer Vision (ICCV). 2011 Pages: 2564-2571.

[22] BIAN J, LIN W, LIU Y, ZHANG L, YEUNG S, CHENG M, REID I. GMS: Grid-Based Motion Statistics for Fast, Ultra-robust Feature Correspondence[J]. international journal of computer vision,2020,128(6): 1580-1593.

[23] G. Li, X. Huang and S. G. Li. A novel circular points-based self-calibration method for a camera's intrinsic parameters using RANSAC[J]. Measurement Science and Technology 2019 Vol. 30 Issue 5.

[24] B. A. Bircher, F. Meli, A. Kung and A. Sofiienko. Traceable x-ray focal spot reconstruction by circular edge analysis: from sub-microfocus to mesofocus[J]. Measurement Science and Technology 2022 Vol. 33 Issue 7.

[25] A. W. Winkler and B. G. Zagar. A curve fitting method for extrinsic camera calibration from a single image of a cylindrical object[J].

[26] B. Li, F. Wang, H. Lv, W. Wu, H. Wei. Microscopic imaging quality evaluation method of single-board computer lens based on pinhole imaging image plane parameter extraction[J]. Applied Optics,2021,42(05):839-847.